Green Chemistry

PAPER

View Article Online
View Journal | View Issue



Cite this: *Green Chem.*, 2020, **22**, 7552

# Integrating Z-scheme heterojunction of $Co_1$-$C_3N_4$@α-$Fe_2O_3$ for efficient visible-light-driven photocatalytic $CO_2$ reduction†

Bing-Cai He, Chao Zhang, Pei-Pei Luo, Yu Li * and Tong-Bu Lu *

Received 20th August 2020,
Accepted 29th September 2020

DOI: 10.1039/d0gc02836c

rsc.li/greenchem

Photocatalytic $CO_2$ reduction coupled with water oxidation provides a fascinating approach to mitigating the issues of global warming and energy shortage. Herein, a direct Z-scheme heterojunction of $Co_1$-$C_3N_4$@α-$Fe_2O_3$ comprising a g-$C_3N_4$-supported single-atomic Co site catalyst (denoted as $Co_1$-$C_3N_4$) and α-$Fe_2O_3$ nanorod arrays is fabricated for efficient $CO_2$ reduction. A CO production rate of 14.9 μmol $g^{-1}$ $h^{-1}$ with a high CO selectivity (>99%) is achieved under visible-light irradiation without any sacrificial agents other than water. Time-resolved photoluminescence (TRPL) analysis reveals that both the Z-scheme mechanism and the single-atomic Co sites contribute to the prolonged lifetime of the photo-induced excitons. Moreover, the formation of the Z-scheme heterojunction would lead to an altered charge density of the single-atomic Co sites. *In situ* diffuse reflectance infrared Fourier-transform spectroscopy and anion adsorption measurements reveal that the key intermediate $CO_2^-$ could be efficiently stabilized by the positively charged Co sites in $Co_1$-$C_3N_4$@α-$Fe_2O_3$, thus enhancing the $CO_2$ reduction performance. This work offers a new direction for the rational design of single-atomic site catalysts in artificial photosynthesis.



## Introduction

The rapidly growing consumption of fossil fuels with excessive emission of $CO_2$ has been contributing to the severe global warming problem and the potential energy shortage.[1,2] Utilizing solar energy to convert $CO_2$ into fuels provides a promising approach to solving the above problems, and scientists have devoted tremendous attention to developing various photocatalysts for $CO_2$ reduction.[3–9] Recently, graphitic carbon nitride (g-$C_3N_4$)-supported single-atomic site catalysts have emerged as remarkable photocatalysts.[10–13] By virtue of the lone pair electrons, the N atoms in the framework can capture various transition metal ions, thus forming single-atomic metal sites on g-$C_3N_4$. In addition, the charge densities of the coordinated metal atoms would be altered by the neighboring N atoms, which may in turn change the adsorption strength and reaction barriers. Density functional theory (DFT) calculations have suggested that single-atomic Pd or Pt loaded on g-$C_3N_4$ can act as effective catalytic sites for photocatalytic $CO_2$ reduction, leading to two different preferential products, HCOOH and $CH_4$, respectively.[14] With the aid of triethylamine (TEA), single-atomic $Co^{2+}$ sites on $C_3N_4$ with different loadings have been successfully synthesized, and the optimized sample with a cobalt loading of 0.128 μmol $mg^{-1}$ exhibits a CO production rate of approximately 25.5 μmol $g^{-1}$ $h^{-1}$ under 60 mW $cm^{-2}$ incident light in the presence of triethanolamine (TEOA) as a sacrificial electron donor.[15] Recently, we have developed an efficient photocatalyst for $CO_2$ reduction by implanting single titanium oxide species on g-$C_3N_4$.[16] In the presence of the $Co(bpy)_3Cl_2$ co-catalyst and TEOA, a CO production rate of 283.9 μmol $g^{-1}$ $h^{-1}$ has been achieved under visible light irradiation. These results strongly demonstrate the viability of g-$C_3N_4$-supported single-atomic site catalysts for photocatalytic $CO_2$ reduction. However, the use of TEOA makes these catalysts less attractive since TEOA is much more expensive than CO. Therefore, it still remains a great challenge to develop low-cost and robust g-$C_3N_4$-based photocatalysts with high efficiency for $CO_2$ conversion using water as an electron source.

Owing to the wide band gap (~2.7 eV), g-$C_3N_4$ can only utilize a marginal portion of visible light ($\lambda$ < 460 nm).[17] Moreover, the water oxidation capacity of g-$C_3N_4$ is poor due to the high energy level of the valence band.[18–20] In this situation, integrating g-$C_3N_4$ with an appropriate semiconductor possessing a narrower band gap and a more positive valence band to establish a Z-scheme heterojunction has been acknowledged

*MOE International Joint Laboratory of Materials Microstructure, Institute for New Energy Materials and Low Carbon Technologies, School of Materials Science & Engineering, Tianjin University of Technology, Tianjin 300384, China. E-mail: yli@email.tjut.edu.cn, lutongbu@tjut.edu.cn*

†Electronic supplementary information (ESI) available. See DOI: 10.1039/d0gc02836c

as an effective strategy, because the Z-scheme heterojunction not only facilitates the spatial separation of the photo-induced electron–hole pairs, but also preserves the maximum capacities for reduction and oxidation of the composites.[20–23]

Herein, we construct a direct Z-scheme heterojunction of $Co_1$-$C_3N_4$@α-$Fe_2O_3$, which composes by single-atomic Co sites loaded on g-$C_3N_4$ ($Co_1$-$C_3N_4$) integrated with α-$Fe_2O_3$ nanorod arrays, for efficient visible-light-driven $CO_2$ reduction coupled with water oxidation. The light-absorption range of $Co_1$-$C_3N_4$ is greatly extended to the entire visible-light region and the lifetime of photo-induced charge carriers is significantly prolonged by the successful incorporation of α-$Fe_2O_3$. Moreover, benefiting from the charge transfer induced by the different Fermi levels between α-$Fe_2O_3$ and $Co_1$-$C_3N_4$, the charge density of single-atomic Co can be further regulated. The results of anion adsorption measurements imply that the stabilization of the critical intermediate $CO_2^-$ is more efficient on the single-atomic Co sites with a higher positive charge. Compared with $Co_1$-$C_3N_4$, the constructed Z-scheme heterojunction shows a substantial improvement for photocatalytic $CO_2$ conversion to CO, with 2.8 times higher than that of $Co_1$-$C_3N_4$ under visible light irradiation and almost 100% CO selectivity.

# Experimental

## Materials

$FeCl_3{\cdot}6H_2O$ (99%, AR) and $CoCl_2{\cdot}6H_2O$ (99%, AR) were purchased from Aladdin. Urea (99%, AR), NaOH (96%, AR) and $Na_2SO_4$ (99%, AR) were purchased from FuChen Chemical Reagent Factory. Nafion 117 solution (~5% in alcohol/water) was purchased from Sigma-Aldrich. $CO_2$ (99.999%) and Ar (99.999%) were purchased from Tianjin Huanyu Gas company. $^{13}CO_2$ (99%) was purchased from Sigma-Aldrich and $H_2{}^{18}O$ (99%) was purchased from Energy Chemical. All chemicals were used as received without further purification. The ultrapure water (Milli-Q water) with an electrical resistivity of 18.2 MΩ cm was used in all experiments.

## Synthetic procedures

The α-$Fe_2O_3$ nanorod arrays were fabricated by a modified strategy reported previously.[24,25] In brief, a piece of fluorine-doped tin oxide (FTO) glass (1 cm × 2.5 cm) was sonicated in acetone, ethanol and water, respectively. Then the FTO glass was leant on the inner side of a Teflon liner with the FTO side facing down. Subsequently, an aqueous solution (15 mL) containing $FeCl_3{\cdot}6H_2O$ (0.51 g) and urea (0.17 g) was added, and the liner was sealed in a stainless steel autoclave, and then heated at 100 °C for 4 h. The as-prepared sample was washed with water and dried by $N_2$ flow to remove redundant sediment. The film was annealed at 550 °C for 2 h and subsequently at 660 °C for 20 min in a muffle furnace with a ramping rate of 2 °C $min^{-1}$, and the α-$Fe_2O_3$ nanorod arrays were finally obtained. The loading amount of the α-$Fe_2O_3$ nanorod arrays was determined to be 0.3 mg by weighing the FTO glass before and after the synthesis.

The g-$C_3N_4$-supported Co single-atom catalyst was prepared by using a two-step strategy.[26] Specifically, urea (15 g) was put into a crucible with a cover, and calcined at 550 °C for 4 h with a ramping rate of 10 °C $min^{-1}$. After cooling down naturally, the product was heated again at 500 °C for 2 h to obtain exfoliated g-$C_3N_4$. For the synthesis of g-$C_3N_4$-supported single-atomic Co site catalyst ($Co_1$-$C_3N_4$), g-$C_3N_4$ (10 mg) was well dispersed in water (10 mL) by vigorous sonication for 30 min. Next, an aqueous solution (500 μL) containing $CoCl_2{\cdot}6H_2O$ (0.336 mM) was dropped into the g-$C_3N_4$ suspension under magnetic stirring. Subsequently, the suspension was stirred for 12 h at 80 °C in an oil bath. The above mixture was then frozen by liquid nitrogen and further dried in vacuum for 48 h by using a lyophilizer. The obtained sample was placed in a porcelain boat and heated to 400 °C for 2 h with a ramping rate of 5 °C $min^{-1}$ under Ar atmosphere. Similar procedures were applied for the synthesis of the g-$C_3N_4$-supported CoO nanoparticle catalyst (CoNP-$C_3N_4$), except that the concentration of $CoCl_2{\cdot}6H_2O$ was increased to 3.36 mM.

To fabricate the Z-scheme system, a well-dispersed aqueous suspension (300 μL) of $Co_1$-$C_3N_4$ (1 mg $mL^{-1}$, 0.3 mg in total) was first drop-coated onto the α-$Fe_2O_3$ nanorod arrays under 60 °C. To strengthen the contact between α-$Fe_2O_3$ and $Co_1$-$C_3N_4$, the sample was transferred to a tube furnace and calcined at 200 °C for 2 h, with a ramping rate of 5 °C $min^{-1}$ under Ar atmosphere. The obtained sample was denoted as $Co_1$-$C_3N_4$@α-$Fe_2O_3$. $C_3N_4$@α-$Fe_2O_3$ and CoNP-$C_3N_4$@α-$Fe_2O_3$ were fabricated according to the same method as that of $Co_1$-$C_3N_4$@α-$Fe_2O_3$, except that $Co_1$-$C_3N_4$ was replaced by g-$C_3N_4$ and CoNP-$C_3N_4$, respectively.

## Characterization

The powder X-ray diffraction (XRD) patterns were recorded by using a Rigaku SmartLab 9 kW with Cu-Kα radiation ($\lambda$ = 1.5418 Å). A Thermo scientific iCAP RQ inductively coupled plasma-mass spectrometer (ICP-MS) was used to determine the Co content. Scanning electron microscopy (SEM) was performed using a FEI Verios 460L scanning electron microscope. Transmission electron microscopy (TEM) images and High-Resolution Transmission Electron Microscopy (HRTEM) images were obtained on FEI Tecnai G2 Spirit Twin and FEI Talos F200X transmission electron microscopes, respectively. Atomic-resolution aberration-corrected high-angle annular dark-field scanning transmission electron microscopy (HAADF-STEM) images and elemental mapping were obtained by using a FEI Titan Themis Cubed G2 60–300 transmission electron microscope. X-ray photoelectron spectroscopy (XPS) measurements were carried out by using a Thermo Scientific ESCALAB250Xi photoelectron spectrometer equipped with Mg Kα (1253.6 eV) as the X-ray source. Ultraviolet–visible (UV–vis) spectroscopic measurements were performed by using a PerkinElmer Lambda 750 UV/VIS/NIR spectrometer. A PerkinElmer Frontier Mid-IR FTIR spectrometer was employed to obtain Fourier-transform infrared spectra. The steady-state photoluminescence spectra (PL) were recorded on a Hitachi F-4600 fluorescence spectrometer. The time-resolved photo-

luminescence (TRPL) curves were recorded using a PicoQuant MicroTime 200 time-resolved confocal fluorescence instrument. The electron spin resonance (ESR) analysis was conducted on an electron paramagnetic resonance spectrometer (Bruker EMXplus-6/1) with 5,5-dimethyl-1-pyrroline *N*-oxide (DMPO) as the trapping agent at 298 K. $CO_2$ adsorption was tested by using a MicrotracBEL BELSORP-Max gas adsorption instrument at 298 K. A Hansatech Chlorolab-2 liquid-phase oxygen measurement system was employed to detect the oxygen evolution during the photocatalytic $CO_2$ reduction.

### Photocatalytic $CO_2$ reduction measurements

Photocatalytic $CO_2$ reduction tests were conducted in a gas–solid setup. A piece of the sample was placed in a 35 mL quartz tube. High-purity $CO_2$ (99.999%) was first passed through water to carry $H_2O$ vapor and then introduced into the quartz tube. The quartz tube was purged with the $CO_2/H_2O$ gas mixture for 30 min and sealed by using a rubber stopper. A 300 W xenon lamp (CEL-HXF300, CEAULIGHT) with a 400 nm cutoff filter was positioned above the sample as the light source. Gaseous products (CO, $CH_4$, and $H_2$) were analysed by using a SHIMADZU GC-2014 gas chromatograph equipped with TCD and FID dual detectors. The products of the $^{13}CO_2$ and $H_2{}^{18}O$ isotopic experiments were analysed by using a Hiden Analytical HPR20 mass spectrometer.

### Photoelectrochemical measurements

All measurements were performed on a CHI 760E electrochemical workstation with a three-electrode setup (working electrode: FTO glass-supported sample; reference electrode: Ag/AgCl electrode; counter electrode: Pt foil) in 0.1 M $Na_2SO_4$ aqueous solution. To measure the photo-current responses, a 300 W Xe lamp (CEL-HXF300, CEAULIGHT) with a 400 nm cutoff filter was used as the light source. A potential of 0.5 V *vs.* Ag/AgCl was applied on the sample and the light was chopped every 10 s to simulate light/dark conditions during the test. Electrochemical impedance spectroscopy (EIS) was carried out in the frequency range of 0.1 MHz to 0.1 Hz with an AC voltage amplitude of 5 mV at an open-circuit potential under visible-light irradiation with a power density of 200 mW $cm^{-2}$.

### *In situ* DRIFTS characterization

*In situ* diffuse reflectance infrared Fourier-transform spectra (DRIFTS) were recorded on a Bruker IFS 66v Fourier-transform spectrometer at the Infrared Spectroscopy and Microspectroscopy Endstation (BL01B) in the National Synchrotron Radiation Laboratory (NSRL), Hefei.[27] The sample was placed in a Harrick diffuse reflectance reaction chamber fixed in the light path. The chamber was equipped with two ZnSe windows and two gas channels. Each spectrum was recorded by 128 scans with a resolution of 4 $cm^{-1}$. The spectrum recorded under Ar atmosphere was set as the background signal.

## Results and discussion

The composite structure comprising α-$Fe_2O_3$ and $Co_1$-$C_3N_4$ was fabricated by a multi-step strategy (Fig. 1a). $Co_1$-$C_3N_4$ exhibits a two-dimensional morphology without any distinguishable clusters, as shown in Fig. 1b and Fig. S1.† The results of elemental mapping indicate the uniform dispersion of Co species on g-$C_3N_4$ (Fig. 1c). The XRD pattern for $Co_1$-$C_3N_4$ also shows no peaks other than those corresponding to g-$C_3N_4$ (Fig. S2†). The atomic dispersion of Co sites was further verified by using a HAADF-STEM image, in which the bright spots represent Co atoms and no aggregation of the bright spots was observed (Fig. 1d).[28] The line-scan profiles also confirm that the Co atoms are well isolated (Fig. S3†). ICP-MS was employed to determine the actual loading of Co. As listed in Table S1,† the mass loading of Co is 0.07% for $Co_1$-$C_3N_4$. A sample comprising CoO nanoparticles on g-$C_3N_4$ was also prepared, with a Co mass loading of 0.81% (denoted as CoNP-$C_3N_4$, Fig. S4†). SEM and TEM images (Fig. 1e and Fig. S5†) show that the α-$Fe_2O_3$ nanorods grown on fluorine-doped tin oxide (FTO) glass have an average length of ~500 nm and an average diameter of ~50 nm. The HRTEM image (Fig. 1f) displays lattice fringes with a lattice spacing of 0.25 nm, which can be assigned to the (110) planes of crystalline α-$Fe_2O_3$. The top view for the composite photocatalyst clearly shows that the α-$Fe_2O_3$ nanorod arrays are covered by highly corrugated $Co_1$-$C_3N_4$ nanosheets (Fig. S6†). Fourier-transform infrared spectrum for $Co_1$-$C_3N_4$ shows a series of characteristic peaks of g-$C_3N_4$ as those reported in the literature (Fig. 1g). Notably, the peak at 806 $cm^{-1}$, which is assigned to the breathing mode of the triazine unit in carbon nitride, is blue-shifted to 808 $cm^{-1}$ when $Co_1$-$C_3N_4$ is integrated with α-$Fe_2O_3$ nanorods.[29] Similar shifts are also found for the peaks at 1200 to 1650 $cm^{-1}$, which correspond to the stretching vibration modes characteristic of aromatic g-$C_3N_4$ heterocycles.[30] The blue shift can be attributed to the charge transfer between $Co_1$-$C_3N_4$ and α-$Fe_2O_3$, which strongly evidences the successful formation of heterojunctions.[21]

UV–vis diffuse reflectance spectroscopy was employed to explore the light-harvesting ability of the as-prepared photocatalysts (Fig. S7†). The absorption edge for $Co_1$-$C_3N_4$@α-$Fe_2O_3$ is significantly extended to 700 nm, covering almost the entire visible region. On the basis of the Tauc plots (Fig. S8†), the band gaps of the α-$Fe_2O_3$ nanorod and $Co_1$-$C_3N_4$ were determined to be 2.12 eV and 2.66 eV, respectively. The energy band structures were further resolved by Mott–Schottky plots (Fig. S9†). The positive slopes of the Mott–Schottky plots indicate the n-type characteristics for both the α-$Fe_2O_3$ nanorod and $Co_1$-$C_3N_4$.[31] The flat band potentials of α-$Fe_2O_3$ and $Co_1$-$C_3N_4$ were calculated to be 0.36 V and −0.94 V *versus* the normal hydrogen electrode (NHE), respectively. For the n-type semiconductor, the flat band potential is close to the bottom of the conduction band (CB).[31,32] Now we are able to draw a clear band diagram for the composite structure, as shown in Fig. 2c. To validate the Z-scheme route for the photo-induced charge carriers, ESR spectroscopy was employed to detect $^{\bullet}OH$

 

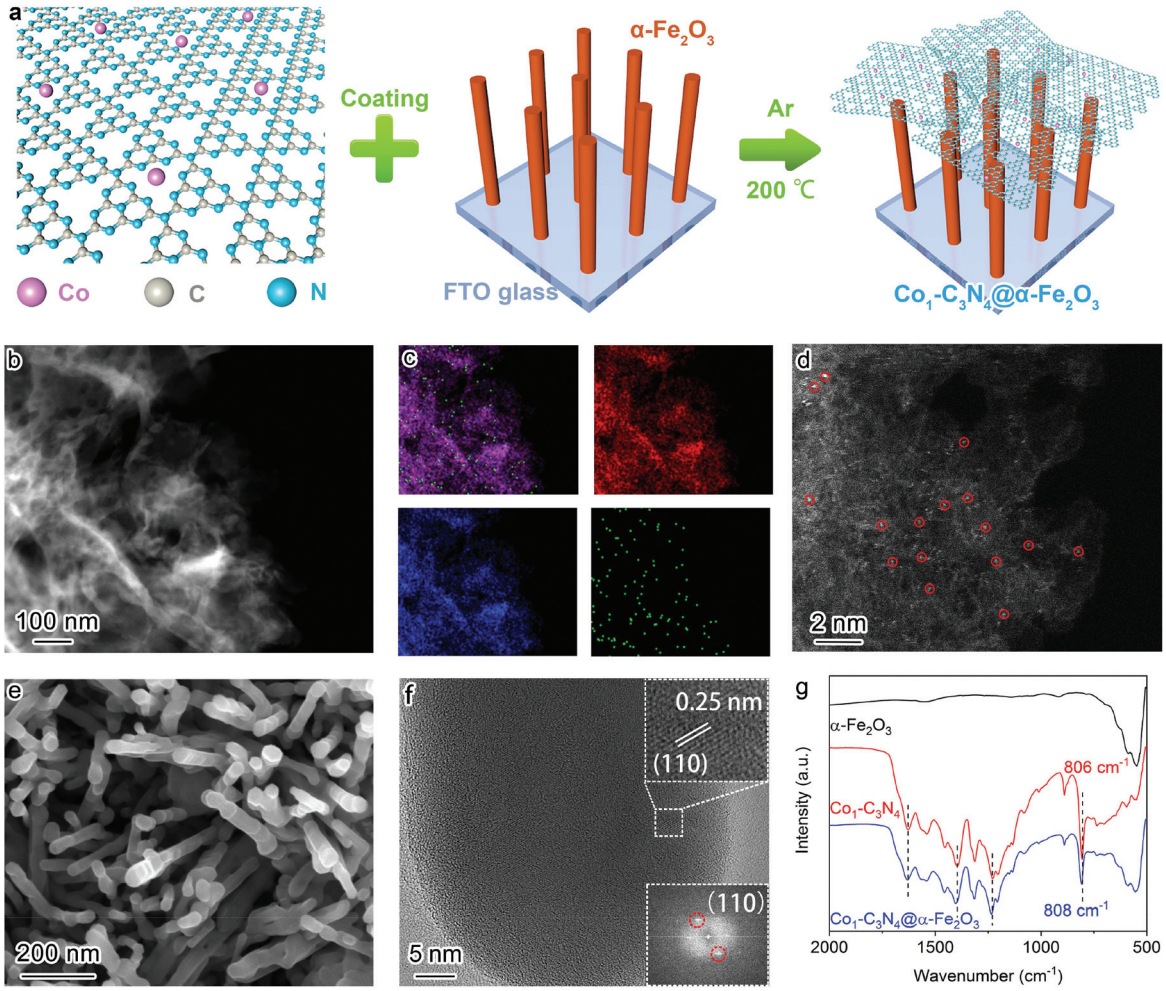


**Fig. 1** (a) Schematic illustration of the fabrication strategy for $Co_1$-$C_3N_4$@α-$Fe_2O_3$. (b) Low-resolution HAADF-STEM image for $Co_1$-$C_3N_4$ and (c) the corresponding elemental mapping images of C (red), N (blue), and Co (green). (d) Atomic-resolution HAADF-STEM image for $Co_1$-$C_3N_4$. The atomically dispersed Co sites are marked in red circles. (e) SEM image and (f) HRTEM image for the α-$Fe_2O_3$ nanorod arrays; insets: lattice fringes of a single α-$Fe_2O_3$ nanorod (top) and the selected area electron diffraction (SAED) pattern (bottom). (g) Fourier-transform infrared spectra for α-$Fe_2O_3$, $Co_1$-$C_3N_4$, and $Co_1$-$C_3N_4$@α-$Fe_2O_3$.

and $^{\bullet}O_2^-$ species with DMPO as the trapping agent (Fig. 2a and b). For pristine α-$Fe_2O_3$, only a weak signal attributed to $^{\bullet}OH$ was observed under visible-light irradiation; for pristine $Co_1$-$C_3N_4$, only the signal attributed to $^{\bullet}O_2^-$ was detected with four identical peaks. These results are understandable by comparing the energy band positions with the reaction potentials of $O_2/^{\bullet}O_2^-$ and $H_2O/^{\bullet}OH$ ($OH^-/^{\bullet}OH$). When $Co_1$-$C_3N_4$@α-$Fe_2O_3$ was employed as the photocatalyst, the signals of both $^{\bullet}OH$ and $^{\bullet}O_2^-$ were observed with much stronger intensities than that for each single component. In addition, neither of the two species was observed for $Co_1$-$C_3N_4$@α-$Fe_2O_3$ under dark conditions (Fig. S10†), suggesting that the reactive oxygen species mentioned above were generated upon incident light. Therefore, we can conclude that the photo-induced charge carriers follow a Z-scheme mechanism rather than a Type II mechanism (Fig. 2c).[8,33]

With the Z-scheme mechanism for $Co_1$-$C_3N_4$@α-$Fe_2O_3$ validated, now we are in a position to investigate the efficacy of the composite structure in promoting photocatalytic $CO_2$ reduction. Fig. 3a shows the average CO evolution rates in $CO_2$ overall splitting for the as-prepared catalysts under visible light ($\lambda$ > 400 nm). No product was detected for α-$Fe_2O_3$ nanorod arrays, as the potential of the conduction band is too positive to trigger the reduction of $CO_2$. The CO production rate for $Co_1$-$C_3N_4$@α-$Fe_2O_3$ was substantially elevated to 14.9 μmol $g^{-1}$ $h^{-1}$, 2.9 times as high as that for $Co_1$-$C_3N_4$ (5.2 μmol $g^{-1}$ $h^{-1}$) and 6.5 times as that for $C_3N_4$@α-$Fe_2O_3$ (2.3 μmol $g^{-1}$ $h^{-1}$). These results imply that the construction of the Z-scheme heterojunction and the introduction of Co favor the photocatalytic reduction of $CO_2$ under visible light. When ultraviolet light was also introduced to the photocatalytic system (by the removal of the cut-off filter), a CO production rate as high as 25.2 μmol $g^{-1}$ $h^{-1}$ was achieved, demonstrating the excellent $CO_2$ reduction capability for $Co_1$-$C_3N_4$@α-$Fe_2O_3$ under full spectrum. To evaluate the utilization efficiency of the solar energy, apparent quantum efficiencies (AQEs) for CO gene-

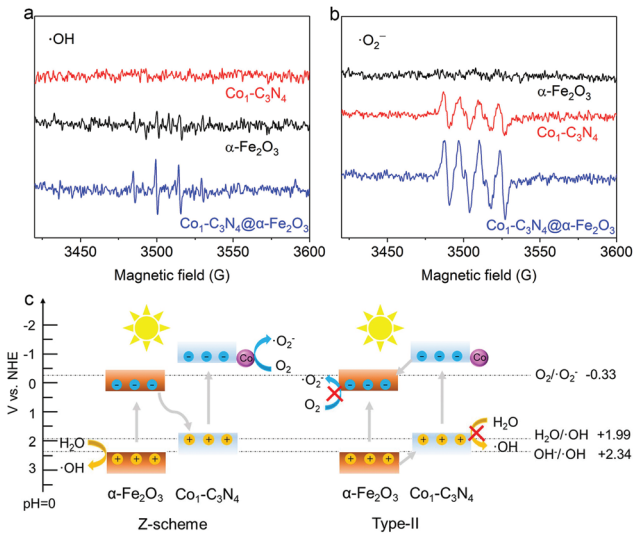


Fig. 2 (a and b) DMPO spin-trapping ESR spectra for $\alpha$-$Fe_2O_3$, $Co_1$-$C_3N_4$, and $Co_1$-$C_3N_4$@$\alpha$-$Fe_2O_3$ under visible-light irradiation. (c) Schematic illustration for the validation of the Z-scheme mechanism rather than Type-II.

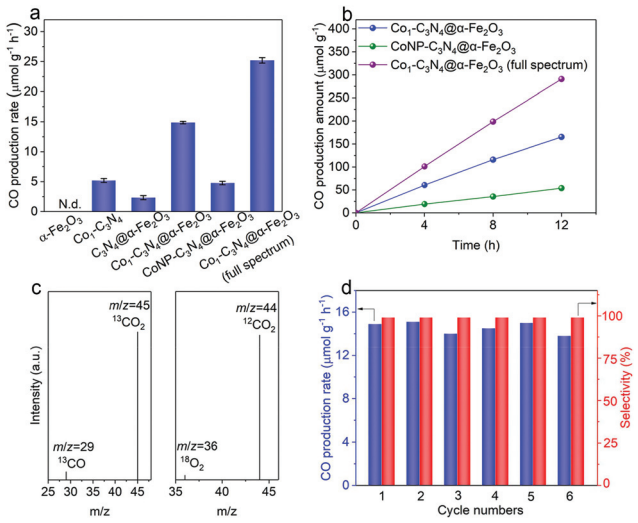


Fig. 3 (a) CO production rates of $\alpha$-$Fe_2O_3$, $Co_1$-$C_3N_4$, $C_3N_4$@$\alpha$-$Fe_2O_3$, $Co_1$-$C_3N_4$@$\alpha$-$Fe_2O_3$, and CoNP-$C_3N_4$@$\alpha$-$Fe_2O_3$; N.d.: not detected. (b) Time-dependent production of CO by CoNP-$C_3N_4$@$\alpha$-$Fe_2O_3$ and $Co_1$-$C_3N_4$@$\alpha$-$Fe_2O_3$. (c) Mass spectra of $^{13}CO$ ($m/z$ = 29) and $^{18}O_2$ ($m/z$ = 36) produced by $Co_1$-$C_3N_4$@$\alpha$-$Fe_2O_3$ in the isotopic experiments. (d) Cycling production of CO for $Co_1$-$C_3N_4$@$\alpha$-$Fe_2O_3$ in photocatalytic $CO_2$ reduction with pure water.

ration were determined under different monochromatic light irradiation (Fig. S11†). The AQEs at 365 nm and 405 nm were determined to be 0.52% and 0.42%, respectively. In addition, it is noteworthy that neither $H_2$ nor $CH_4$ was detected in the gaseous products for a continuous 12-hour photocatalytic test, suggesting the high selectivity for CO (Fig. 3b). To the best of our knowledge, the performance of $Co_1$-$C_3N_4$@$\alpha$-$Fe_2O_3$ here is among the top levels in comparison with other g-$C_3N_4$-based and single-atomic site catalysts in photocatalytic $CO_2$ coupled with water oxidation (Table S5†). To further examine the essentialness of the single-atomic character of Co in $CO_2$ reduction, CoNP-$C_3N_4$@$\alpha$-$Fe_2O_3$ was employed for comparison. The result shows that the CO production rate for CoNP-$C_3N_4$@$\alpha$-$Fe_2O_3$ is much lower (4.8 μmol $g^{-1}$ $h^{-1}$), suggesting the critical role of single-atomic Co sites in photocatalytic $CO_2$ reduction. A similar irradiation test under Ar atmosphere was conducted on $Co_1$-$C_3N_4$@$\alpha$-$Fe_2O_3$, and no CO was detected. To further identify the origin of CO, we traced the carbon source in the reduction process using a $^{13}C$ isotopic label. Fig. 3c shows the mass spectrum of CO obtained with $^{13}CO_2$ as a substrate under identical photocatalytic reaction conditions; a distinct $^{13}CO$ peak ($m/z$ = 29) was observed, indicating that the CO indeed originates from $CO_2$. $H_2{}^{18}O$, instead of $H_2{}^{16}O$, was also adopted to verify the water oxidation half-reaction, and a clear $^{18}O_2$ peak ($m/z$ = 36) was observed in the mass spectrum. Moreover, molecular oxygen was detected as the product by liquid-phase oxygen measurement system, further confirming that the $CO_2$ reduction is coupled with water oxidation (Fig. S12†). As shown in Fig. 3d and S13,† the production rate and selectivity of CO for $Co_1$-$C_3N_4$@$\alpha$-$Fe_2O_3$ remained almost unchanged during the six consecutive cycles (4 h each), and no aggregation of Co species appeared after the stability test, validating the excellent stability for the Z-scheme system under visible light.

Given the above results, a question naturally arises: What role does the Z-scheme play in enhancing the photocatalytic $CO_2$ reduction? In addition to the significantly broadened light-absorption range, the dynamic behaviors of the photo-induced charge carriers are also effectively regulated. The photocurrent responses were recorded under intermittent visible-light irradiation in 0.1 M $Na_2SO_4$ aqueous solution (Fig. S14†). The photocurrent density for $Co_1$-$C_3N_4$@$\alpha$-$Fe_2O_3$ is higher than those for $\alpha$-$Fe_2O_3$ and $Co_1$-$C_3N_4$, suggesting the more efficient photo-induced electron–hole separation for improved $CO_2$ reduction.[34] Electrochemical impedance spectroscopy (EIS) was conducted to reflect the charge transfer resistance (Fig. S15†). The Nyquist plots reveal that $Co_1$-$C_3N_4$@$\alpha$-$Fe_2O_3$ has the lowest charge transfer resistance, which is beneficial for the separation and migration of the photo-induced charge carriers.[24,35] To investigate the lifetime of the electron–hole pairs, we employed PL spectroscopy. As shown in Fig. S16,† the main emission peak located at 442 nm can be ascribed to the inter-band recombination of photo-induced charge carriers. The dramatically quenched PL intensity for $Co_1$-$C_3N_4$@$\alpha$-$Fe_2O_3$ indicates the faster electron migration and the efficient suppression of the carrier recombination.[29] To gain in-depth information for the carrier dynamics, TRPL decay curves for the as-prepared photocatalysts were recorded. As revealed in Fig. 4a and S17,† $Co_1$-$C_3N_4$@$\alpha$-$Fe_2O_3$ shows a significantly slower decay kinetics than $\alpha$-$Fe_2O_3$ and $Co_1$-$C_3N_4$. The PL lifetimes are listed in Table S2.† The shorter lifetime $\tau_1$ is related to the non-radiative relaxation, and the longer lifetime $\tau_2$ is attributed to the inter-band recombination of the photo-induced excitons, which mainly contributes to the

 

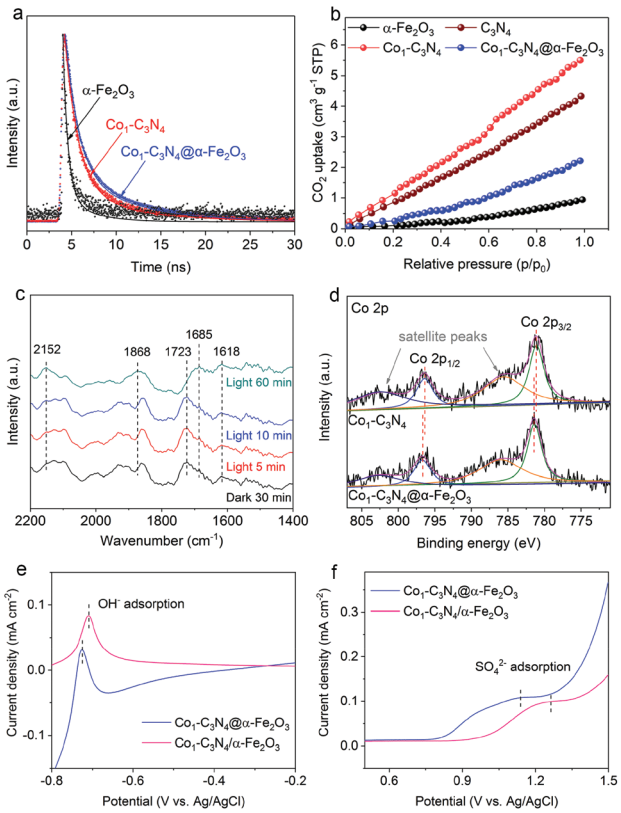


**Fig. 4** (a) TRPL decay curves for $\alpha$-$Fe_2O_3$, $Co_1$-$C_3N_4$, and $Co_1$-$C_3N_4$@$\alpha$-$Fe_2O_3$. (b) $CO_2$ adsorption isotherms for $\alpha$-$Fe_2O_3$, g-$C_3N_4$, $Co_1$-$C_3N_4$, and $Co_1$-$C_3N_4$@$\alpha$-$Fe_2O_3$. (c) *In situ* DRIFTS spectra for $Co_1$-$C_3N_4$@$\alpha$-$Fe_2O_3$ under different irradiation conditions with the existence of $CO_2$ and $H_2O$. (d) X-ray photoelectron spectroscopy spectra of the Co 2p core levels for $Co_1$-$C_3N_4$ and $Co_1$-$C_3N_4$@$\alpha$-$Fe_2O_3$. Single oxidative LSV scans at 100 mV $s^{-1}$ in (e) Ar-bubbled 0.5 M NaOH and (f) Ar-bubbled 0.1 M $Na_2SO_4$ for $Co_1$-$C_3N_4$@$\alpha$-$Fe_2O_3$ and $Co_1$-$C_3N_4$/$\alpha$-$Fe_2O_3$, respectively.

photoluminescence.[21] Notably, the average lifetime ($\tau$) of $Co_1$-$C_3N_4$@$\alpha$-$Fe_2O_3$ is prolonged to 5.17 ns, suggesting the high efficacy of the Z-scheme heterojunction. Specifically, the photo-induced electrons in the conduction band of $\alpha$-$Fe_2O_3$ can efficiently annihilate the holes in the valence band of $Co_1$-$C_3N_4$, thus suppressing the recombination of photo-induced excitons inside each component. As a consequence, more photo-induced electrons would be preserved on the conduction band of $Co_1$-$C_3N_4$, and more photo-induced holes would be preserved on the valence band of $\alpha$-$Fe_2O_3$, thus leading to superior photocatalytic performances. Furthermore, the incorporation of single-atomic Co sites also results in prolonged average lifetimes with significantly altered $\tau_1$ and $\tau_2$. The atomically dispersed Co can act as effective trap sites to capture the photo-induced electrons from the conduction band of g-$C_3N_4$, thereby inhibiting the recombination of the electrons with the VB holes.[36,37] Therefore, for $Co_1$-$C_3N_4$@$\alpha$-$Fe_2O_3$, the Z-scheme structure and the single-atomic Co sites collaboratively contribute to the efficient separation of the photo-induced excitons.

To shed light on the role of single-atomic Co sites at the catalytic interface during photocatalytic $CO_2$ reduction, $CO_2$ adsorption was employed to determine the chemisorption capacities of these catalysts. As depicted in Fig. 4b, $Co_1$-$C_3N_4$ adsorbs a much larger amount of $CO_2$ than bare g-$C_3N_4$, suggesting the efficacy of the single-atomic Co sites. It is also worth pointing out that the integration of $\alpha$-$Fe_2O_3$ significantly reduces the $CO_2$ uptake, which can be attributed to the poor $CO_2$ adsorption ability of $\alpha$-$Fe_2O_3$ nanorod arrays. To unravel the possible reaction pathway that occurs on $Co_1$-$C_3N_4$@$\alpha$-$Fe_2O_3$, we carried out *in situ* DRIFTS measurements to explore the key intermediates in photocatalytic $CO_2$ reduction. As illustrated in Fig. 4c, the peaks at 1618 $cm^{-1}$, 1723 $cm^{-1}$, and 1868 $cm^{-1}$ can be assigned to bidentate carbonate (b-$CO_3^{2-}$), chelating bridged carbonate (c-$CO_3^{2-}$), and multi-bonded CO (m-CO) on the g-$C_3N_4$ substrate, respectively.[38,39] The carbonate species are formed by the interaction of the surface O atoms of g-$C_3N_4$ with adsorbed $CO_2$.[38] During the 60 min irradiation, the peak intensity of b-$CO_3^{2-}$ remained unchanged, whereas the peak intensity of c-$CO_3^{2-}$ significantly decreased. Meanwhile, an obvious increase was observed in the m-CO peak. These results can be explained by the catalytic effect that c-$CO_3^{2-}$ is converted into m-CO during the photocatalytic $CO_2$ reduction. More importantly, a peak at 2152 $cm^{-1}$ emerged and the intensity of the peak gradually increased with the irradiation time. This peak can be assigned to the stretching vibration of CO adsorbed on an isolated Co site.[40,41] This result further highlights the key role of the single-atomic Co sites in CO evolution. Moreover, another peak at 1685 $cm^{-1}$ attributed to $CO_2^-$ adsorbed on Co sites was observed, the intensity of which noticeably increased after 60 min irradiation.[38,42] Therefore, it can be inferred that the $CO_2$-to-CO conversion on the isolated Co sites proceeds *via* the formation of $CO_2^-$, which is generally regarded as the rate-determining step in $CO_2$ reduction.[4,43–45] The stabilization of $CO_2^-$ has a great impact on the overall performance of the photocatalytic $CO_2$ reduction, and largely depends on the local charge density of the active sites.[46–48] In our Z-scheme heterojunction, the electrons in $Co_1$-$C_3N_4$ with a relatively high Fermi level would spontaneously migrate to $\alpha$-$Fe_2O_3$ to eliminate the disparity between the Fermi levels,[34] which was verified by XPS analysis in Fig. S18† and Fig. 4c. The N 1s spectrum for $Co_1$-$C_3N_4$ can be deconvoluted into three peaks located at 398.3 eV (C–N=C), 400 eV (N–(C)$_3$) and 401.3 eV (C–N–H$_x$), respectively.[13,49] Notably, these peaks shift to higher binding energies after assembly with $\alpha$-$Fe_2O_3$ (Table S3†). Moreover, distinguishable shifts in similar trend were also observed for Co $2p_{3/2}$ peaks (Table S3†).[13,50] In contrast, in terms of the binding energy of Fe, the Fe 2p peaks of the Z-scheme heterojunction downshift by 0.2 eV relative to those of pristine $\alpha$-$Fe_2O_3$ (Fig. S19 and Table S4†).[51] This result is indicative of a partial electron transfer from N and Co to Fe, confirming the electron migration direction between the two components.[52,53] Accordingly, the Co species in $Co_1$-$C_3N_4$@$\alpha$-$Fe_2O_3$ exhibits a higher oxidation state than that in $Co_1$-$C_3N_4$. In this case, the negatively charged $CO_2^-$ can be better stabilized by the electro-

static interaction with the more positively charged Co sites.[45] To confirm the superiority of $Co_1$-$C_3N_4$@α-$Fe_2O_3$ in $CO_2^-$ stabilization, the adsorption of $OH^-$ and $SO_4^{2-}$ (as proper surrogates for $CO_2^-$) was conducted.[54–56] In order to eliminate any possible disturbance, we prepared a non-heterojunction mixture comprising α-$Fe_2O_3$ nanorod arrays and $Co_1$-$C_3N_4$ with the assistance of Nafion solution rather than *via* the subsequent thermal treatment (denoted as $Co_1$-$C_3N_4$/α-$Fe_2O_3$). The oxidative linear sweep voltammograms (LSV) in NaOH aqueous solution reveal that the potential of $OH^-$ adsorption for $Co_1$-$C_3N_4$@α-$Fe_2O_3$ is 19 mV lower than that for $Co_1$-$C_3N_4$/α-$Fe_2O_3$ (Fig. 4e). This difference becomes more prominent in the adsorption of $SO_4^{2-}$. As shown in Fig. 4f, a potential of 1.14 V *vs.* Ag/AgCl is required for the adsorption of $SO_4^{2-}$ on $Co_1$-$C_3N_4$@α-$Fe_2O_3$, 120 mV lower than that on $Co_1$-$C_3N_4$/α-$Fe_2O_3$ (1.26 V *vs.* Ag/AgCl). Since the lower potential implies a stronger binding of the anion, these results strongly indicate that the Z-scheme $Co_1$-$C_3N_4$@α-$Fe_2O_3$ can efficiently stabilize the key intermediate $CO_2^-$, thereby facilitating CO evolution.

## Conclusions

In summary, we have constructed a Z-scheme heterojunction of $Co_1$-$C_3N_4$@α-$Fe_2O_3$ comprising $Co_1$-$C_3N_4$ and α-$Fe_2O_3$ nanorod arrays for efficient visible-light-driven $CO_2$ reduction coupled with water oxidation. The introduction of the Z-scheme heterojunction into a single-atomic catalyst of $Co_1$-$C_3N_4$ not only promotes the separation of the photo-induced charge carriers for benefiting $CO_2$ reduction, but also enhances the capability of water oxidation. XPS analysis reveals that the single-atomic Co sites in $Co_1$-$C_3N_4$ become more positively charged after the formation of the heterojunction, which contributes to the efficient stabilization of $CO_2^-$ and hence facilitates the $CO_2$ reduction, as verified by the *in situ* DRIFTS spectra and anion adsorption test. As a result, a CO generation rate of 14.9 μmol $g^{-1}$ $h^{-1}$ with over 99% CO selectivity is achieved under visible-light irradiation using water as an electron source. Our findings here underline the importance of the charge regulation on single-atomic sites by the Z-scheme heterojunction for enhancing catalytic performances, and offer a new approach to developing high-efficiency single-atomic site catalysts for artificial photosynthesis.

## Conflicts of interest

There are no conflicts to declare.

## Acknowledgements

This work was supported by the National Key R&D Program of China (2017YFA0700104), the National Natural Science Foundation of China (21931007, 21905204, 21805207) and 111 Project of China (D17003). *In situ* DRIFTS measurements were performed at the Infrared Spectroscopy and Microspectroscopy Endstation (BL01B) in the National Synchrotron Radiation Laboratory (NSRL) in Hefei, China.

## References

1 C. F. Shih, T. Zhang, J. Li and C. Bai, *Joule*, 2018, **2**, 1925–1949.
2 O. S. Bushuyev, P. De Luna, C. T. Dinh, L. Tao, G. Saur, J. van de Lagemaat, S. O. Kelley and E. H. Sargent, *Joule*, 2018, **2**, 825–832.
3 S. C. Roy, O. K. Varghese, M. Paulose and C. A. Grimes, *ACS Nano*, 2010, **4**, 1259–1278.
4 S. N. Habisreutinger, L. Schmidt-Mende and J. K. Stolarczyk, *Angew. Chem., Int. Ed.*, 2013, **52**, 7372–7408.
5 J. Ran, M. Jaroniec and S. Z. Qiao, *Adv. Mater.*, 2018, **30**, 1704649.
6 J. Di, C. Zhu, M. Ji, M. Duan, R. Long, C. Yan, K. Gu, J. Xiong, Y. She, J. Xia, H. Li and Z. Liu, *Angew. Chem., Int. Ed.*, 2018, **57**, 14847–14851.
7 X. Li, Y. Sun, J. Xu, Y. Shao, J. Wu, X. Xu, Y. Pan, H. Ju, J. Zhu and Y. Xie, *Nat. Energy*, 2019, **4**, 690–699.
8 Z. Jiang, W. Wan, H. Li, S. Yuan, H. Zhao and P. K. Wong, *Adv. Mater.*, 2018, **30**, 1706108.
9 Y. Jiang, J.-F. Liao, H.-Y. Chen, H.-H. Zhang, J.-Y. Li, X.-D. Wang and D.-B. Kuang, *Chem*, 2020, **6**, 766–780.
10 Y. Li, Z. Wang, T. Xia, H. Ju, K. Zhang, R. Long, Q. Xu, C. Wang, L. Song, J. Zhu, J. Jiang and Y. Xiong, *Adv. Mater.*, 2016, **28**, 6959–6965.
11 X. Li, W. Bi, L. Zhang, S. Tao, W. Chu, Q. Zhang, Y. Luo, C. Wu and Y. Xie, *Adv. Mater.*, 2016, **28**, 2427–2431.
12 Y. Cao, S. Chen, Q. Luo, H. Yan, Y. Lin, W. Liu, L. Cao, J. Lu, J. Yang, T. Yao and S. Wei, *Angew. Chem., Int. Ed.*, 2017, **56**, 12191–12196.
13 W. Liu, L. Cao, W. Cheng, Y. Cao, X. Liu, W. Zhang, X. Mou, L. Jin, X. Zheng, W. Che, Q. Liu, T. Yao and S. Wei, *Angew. Chem., Int. Ed.*, 2017, **56**, 9312–9317.
14 G. Gao, Y. Jiao, E. R. Waclawik and A. Du, *J. Am. Chem. Soc.*, 2016, **138**, 6292–6297.
15 P. Huang, J. Huang, S. A. Pantovich, A. D. Carl, T. G. Fenton, C. A. Caputo, R. L. Grimm, A. I. Frenkel and G. Li, *J. Am. Chem. Soc.*, 2018, **140**, 16042–16047.
16 S. Tang, X. Yin, G. Wang, X. Lu and T. Lu, *Nano Res.*, 2019, **12**, 457–462.
17 X. Wang, K. Maeda, A. Thomas, K. Takanabe, G. Xin, J. M. Carlsson, K. Domen and M. Antonietti, *Nat. Mater.*, 2009, **8**, 76–80.
18 J. Zhang, X. Chen, K. Takanabe, K. Maeda, K. Domen, J. D. Epping, X. Fu, M. Antonietti and X. Wang, *Angew. Chem., Int. Ed.*, 2010, **49**, 441–444.
19 J. Zhang, J. Sun, K. Maeda, K. Domen, P. Liu, M. Antonietti, X. Fu and X. Wang, *Energy Environ. Sci.*, 2011, **4**, 675–678.
20 W.-J. Ong, L.-L. Tan, Y. H. Ng, S.-T. Yong and S.-P. Chai, *Chem. Rev.*, 2016, **116**, 7159–7329.

 

21 Z. Zhang, J. Huang, Y. Fang, M. Zhang, K. Liu and B. Dong, *Adv. Mater.*, 2017, **29**, 1606688.
22 Y. Wang, H. Suzuki, J. Xie, O. Tomita, D. J. Martin, M. Higashi, D. Kong, R. Abe and J. Tang, *Chem. Rev.*, 2018, **118**, 5201–5241.
23 Y.-F. Mu, W. Zhang, G.-X. Dong, K. Su, M. Zhang and T.-B. Lu, *Small*, 2020, **16**, 2002140.
24 P. Kuang, L. Zhang, B. Cheng and J. Yu, *Appl. Catal., B*, 2017, **218**, 570–580.
25 S.-S. Yi, J.-M. Yan and Q. Jiang, *J. Mater. Chem. A*, 2018, **6**, 9839–9845.
26 S. Cao, H. Li, T. Tong, H.-C. Chen, A. Yu, J. Yu and H. M. Chen, *Adv. Funct. Mater.*, 2018, **28**, 1802169.
27 C. Hu, X. Wang, Z. Qi and C. Li, *Infrared Phys. Technol.*, 2020, **105**, 103200.
28 P. Huang, M. Cheng, H. Zhang, M. Zuo, C. Xiao and Y. Xie, *Nano Energy*, 2019, **61**, 428–434.
29 X. She, J. Wu, H. Xu, J. Zhong, Y. Wang, Y. Song, K. Nie, Y. Liu, Y. Yang, M.-T. F. Rodrigues, R. Vajtai, J. Lou, D. Du, H. Li and P. M. Ajayan, *Adv. Energy Mater.*, 2017, **7**, 1700025.
30 M. J. Bojdys, J.-O. Müller, M. Antonietti and A. Thomas, *Chem. – Eur. J.*, 2008, **14**, 8177–8182.
31 M. Shi, G. Li, J. Li, X. Jin, X. Tao, B. Zeng, E. A. Pidko, R. Li and C. Li, *Angew. Chem.*, 2020, **59**, 6590–6595.
32 Y. Zhou, L. Zhang and W. Wang, *Nat. Commun.*, 2019, **10**, 506.
33 S. Cao, J. Low, J. Yu and M. Jaroniec, *Adv. Mater.*, 2015, **27**, 2150–2176.
34 S. Bai, J. Jiang, Q. Zhang and Y. Xiong, *Chem. Soc. Rev.*, 2015, **44**, 2893–2939.
35 Y. Li, S. Chen, D. Xi, Y. Bo, R. Long, C. Wang, L. Song and Y. Xiong, *Small*, 2018, **14**, 1702109.
36 Y. Yang, F. Li, J. Chen, J. Fan and Q. Xiang, *ChemSusChem*, 2020, **13**, 1979–1985.
37 S. Ji, Y. Qu, T. Wang, Y. Chen, G. Wang, X. Li, J. Dong, Q. Chen, W. Zhang, Z. Zhang, S. Liang, R. Yu, Y. Wang, D. Wang and Y. Li, *Angew. Chem.*, 2020, **59**, 10651–10657.
38 L. Liu, Y. Jiang, H. Zhao, J. Chen, J. Cheng, K. Yang and Y. Li, *ACS Catal.*, 2016, **6**, 1097–1108.
39 Q.-S. Chen, S.-G. Sun, Z.-Y. Zhou, Y.-X. Chen and S.-B. Deng, *Phys. Chem. Chem. Phys.*, 2008, **10**, 3645–3654.
40 J. Jansson, A. E. C. Palmqvist, E. Fridell, M. Skoglundh, L. Österlund, P. Thormählen and V. Langer, *J. Catal.*, 2002, **211**, 387–397.
41 H.-K. Lin, C.-B. Wang, H.-C. Chiu and S.-H. Chien, *Catal. Lett.*, 2003, **86**, 63–68.
42 X. Zu, X. Li, W. Liu, Y. Sun, J. Xu, T. Yao, W. Yan, S. Gao, C. Wang, S. Wei and Y. Xie, *Adv. Mater.*, 2019, **31**, e1808135.
43 Y. Chen, C. W. Li and M. W. Kanan, *J. Am. Chem. Soc.*, 2012, **134**, 19969–19972.
44 Ș. Neațu, J. A. Maciá-Agulló, P. Concepción and H. Garcia, *J. Am. Chem. Soc.*, 2014, **136**, 15969–15976.
45 A. Wuttig, M. Yaguchi, K. Motobayashi, M. Osawa and Y. Surendranath, *Proc. Natl. Acad. Sci. U. S. A.*, 2016, **113**, E4585–E4593.
46 I. V. Chernyshova, P. Somasundaran and S. Ponnurangam, *Proc. Natl. Acad. Sci. U. S. A.*, 2018, **115**, E9261–E9270.
47 Y. Hori, H. Wakebe, T. Tsukamoto and O. Koga, *Electrochim. Acta*, 1994, **39**, 1833–1839.
48 M. R. Singh, J. D. Goodpaster, A. Z. Weber, M. Head-Gordon and A. T. Bell, *Proc. Natl. Acad. Sci. U. S. A.*, 2017, **114**, E8812–E8821.
49 J. Liu, H. Shi, Q. Shen, C. Guo and G. Zhao, *Green Chem.*, 2017, **19**, 5900–5910.
50 Q. Song, J. Li, L. Wang, Y. Qin, L. Pang and H. Liu, *J. Catal.*, 2019, **370**, 176–185.
51 Q. Xu, B. Zhu, C. Jiang, B. Cheng and J. Yu, *Sol. RRL*, 2018, **2**, 1800006.
52 Y.-X. Liu, H.-H. Wang, T.-J. Zhao, B. Zhang, H. Su, Z.-H. Xue, X.-H. Li and J.-S. Chen, *J. Am. Chem. Soc.*, 2018, **141**, 38–41.
53 B. Jiang, X.-G. Zhang, K. Jiang, D.-Y. Wu and W.-B. Cai, *J. Am. Chem. Soc.*, 2018, **140**, 2880–2889.
54 A. Salehi-Khojin, H.-R. M. Jhong, B. A. Rosen, W. Zhu, S. Ma, P. J. A. Kenis and R. I. Masel, *J. Phys. Chem. C*, 2013, **117**, 1627–1632.
55 F. Lei, W. Liu, Y. Sun, J. Xu, K. Liu, L. Liang, T. Yao, B. Pan, S. Wei and Y. Xie, *Nat. Commun.*, 2016, **7**, 12697.
56 X. Wang, Z. Chen, X. Zhao, T. Yao, W. Chen, R. You, C. Zhao, G. Wu, J. Wang, W. Huang, J. Yang, X. Hong, S. Wei, Y. Wu and Y. Li, *Angew. Chem., Int. Ed.*, 2018, **57**, 1944–1948.